Journal of Marine Research, 54, 261–284, 1996

Seasonal transport variations of the wind-driven ocean circulation in a two-layer planetary geostrophic model with a continental slope

by Toshihiro Sakamoto[1] and Toshio Yamagata[1]

ABSTRACT

Using a simple two-layer planetary geostrophic model with a continental slope, the observed seasonal variation of the total transport of the Kuroshio is explained qualitatively for the first time in a quite concise way. During the period of weak winds in summer, the total transport is much larger than the nontopographic Sverdrup transport. This is because the joint effect of baroclinicity and bottom relief (so-called JEBAR) drives the barotropic flow with releasing the available potential energy accumulated in winter. In winter, on the other hand, the transport is much smaller than the nontopographic Sverdrup transport. This is mainly due to the topographic beta-effect. In addition to the available potential energy supplied directly by winds, the barotropic flow excited by the strong winds in winter impinges on the bottom slope to induce the baroclinic flow so that the wind-driven barotropic flow is converted into the available potential energy to be released in summer. Thus, the role of JEBAR is to make the total transport of the Kuroshio relatively insensitive to seasonal changes of winds as observed. This mechanism may be called "JEBAR rectification" for simplicity.

1. Introduction

The seasonal variation in the total transport of the Kuroshio is known to be much smaller than that in the nontopographic Sverdrup transport calculated by using the wind stresses over the entire North Pacific. Although available data are limited, the observed transport appears to be much less than the Sverdrup transport in winter when the wind forcing is strong. In addition, the seasonal change in the Kuroshio transport seems to be almost 180° out of phase with that predicted by the Sverdrup balance (Fig. 1). These characteristics cannot be explained by the classical quasi-steady Sverdrup theory (cf. Sekine and Kutsuwada, 1994). The seasonal variation in the observed transport of the Florida Current is also much smaller than (and almost opposite phase to) that predicted by the Sverdrup balance (Niiler and Richardson, 1973). Anderson and Corry (1985a), using a linear, wind-driven two-layer model with idealized geometry and bottom topography, find that the seasonal variation in the western boundary current depends on the relation between the periods of winds and

1. Department of Earth and Planetary Physics, Graduate School of Science, The University of Tokyo, Tokyo 113, Japan.

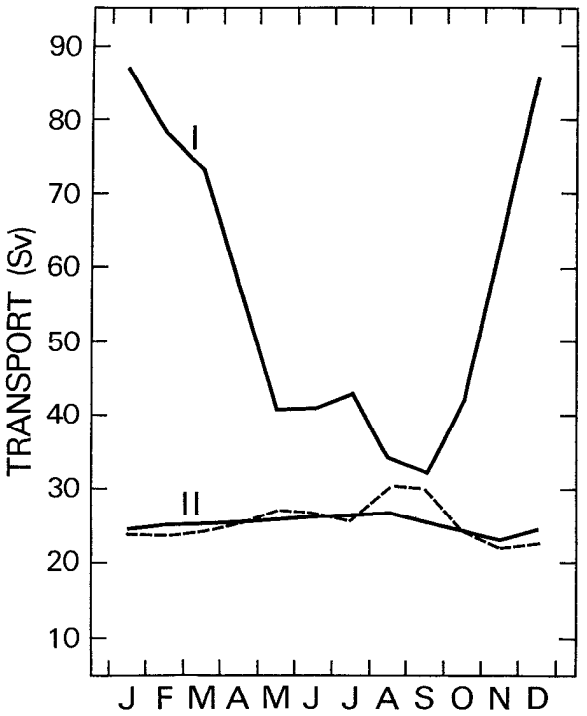

Figure 1. Annual cycle of the Kuroshio transport. The solid line I denotes the nontopographic Sverdrup transport calculated using the monthly mean climatological winds of Hellerman and Rosenstein (1983). The solid line II denotes the geostrophic transport above 700 db across the PN-line near the Ryukyu Islands. The hydrographic data from 1973 through 1992 are used for the dynamic calculation (courtesy of the Nagasaki Marine Observatory). The dashed line denotes the transport above 700 db across the PN-line from a preliminary result of a recent high-resolution ocean general circulation model (Kagimoto and Yamagata, private communication).

the time taken for the wind-generated planetary waves to pass over the topography. Anderson and Corry (1985b) run a similar two-layer model in the presence of realistic bottom topography with the observed seasonal winds for the North Atlantic; they are successful in showing the summer maximum of transport. However, the detailed mechanism appears to be left unanswered.

Our motivation for the present article stems from the above discrepancy between the observed transport variations and those predicted by the Sverdrup balance. In particular, we focus on the question why the observed Kuroshio transport shows the seasonal variation much weaker than that predicted by the Sverdrup theory. We try to explain the above phenomenon within a framework of the classical wind-driven circulation theory by taking into account the interaction between rotational stratified flow and bottom topography. For this purpose, we adopt a highly idealized model:

the model ocean is composed of a square basin with two immiscible layers and either western or northern continental slope. As a forcing, we adopt zonal wind stresses of moderate intensity so that geostrophic contours of the lower layer are not closed. In addition, no outcropping is allowed and the bottom slope is assumed to be always immersed in the lower layer. The planetary geostrophic equations are used as the governing equations because of their simplicity (cf. Salmon, 1986; 1992). The model set-up is described in detail in Section 2.

Assuming the above conditions, Anderson and Killworth's (1977) one-dimensional, linear spin-up theory with bottom topography provides a guide to understanding our experiment. As a consequence of propagation of baroclinic long planetary waves, the steady state of our model ocean must be such that the wind-driven current is confined only in the upper layer to which the external forcing is applied directly (Veronis, 1973). This means that the lower layer is in no-motion. Thus, we expect that the ocean interior is governed by the nontopographic Sverdrup balance despite the existence of bottom topography. This process is confirmed both analytically and numerically in Section 3. It is demonstrated that the process of *compensation* in the lower layer is due to barotropic-baroclinic interaction through the bottom topography.

The lower layer may be in motion in the steady state if we include such processes as interfacial friction between two adjacent layers (cf. Welander, 1966), closed geostrophic contours (cf. Rhines and Young, 1982), outcropping (cf. Luyten *et al.,* 1983; Salmon, 1994), diapycnal mixing (cf. McCreary, 1981) and thermohaline circulations (cf. Stommel *et al.,* 1958; Holland, 1973). These processes may lead to noncompensation of horizontal pressure gradients and hence produce bottom pressure torque by interacting with bottom topography in the vorticity balance (Welander, 1959; Gates, 1966). The extra forcing in addition to the wind stress curl can either increase or decrease the Sverdrup transport. In other words, the vorticity input from the rotating solid earth via bottom topography may exceed that from the atmosphere.

The above process of compensation via topography and the role played by the bottom pressure torque due to noncompensated flow over topography may be unified into the concept of JEBAR (or JEBAT) (Joint Effect of BAroclinicity and bottom Relief (Topography)). The acronym in the bracket was coined by Sarkisyan (1969). This aspect of JEBAR is shown clearly by Mertz and Wright (1992) in their analytical study using a linear, continuously stratified model. The formulation of the JEBAR term for layered models, which is our present concern, is shown in the Appendix. The JEBAR term appears explicitly in a vorticity equation derived from the vertically averaged momentum equations (Huthnance, 1984; Mertz and Wright, 1992), and obviously plays a role in completing compensation in deep layers. In this sense, the JEBAR term works just as a virtual forcing like the wind stress curl as shown in Section 3.

The concept of JEBAR has been introduced in diagnostic studies as a mechanism

which may double the Gulf Stream transport predicted using the classical theory established by Stommel (1948), Hidaka (1949) and Munk (1950) (Sarkisyan and Ivanov, 1971). The Russian school's extensive studies on those diagnostic calculations during the 1960s and 1970s are reviewed in detail by Sarkisyan (1977). Their attempt turned out to be successful as shown by Holland and Hirschman (1972). However, the first succinct demonstration of the important interaction between baroclinicity and topography awaited Holland (1973). Using a prognostic three-dimensional model with a western continental slope, Holland (1973) finds that the buoyancy-driven meridional circulation induces a horizontal recirculation over the slope due to vortex-shrinking; the enhancement of the total transport of the western boundary current is rather dramatic compared with the nontopographic Sverdrup transport.

So far, the concept of JEBAR has been mostly appreciated in regard to the thermohaline processes in the Atlantic in the context of a climatological mean state (Mellor *et al.*, 1982) and a long-term variation (Greatbatch *et al.*, 1991). This is not the case with our present model in which no thermohaline processes are assumed. Instead, we will show for the first time that varying wind-driven circulations with baroclinicity and bottom topography may be more easily understood in terms of the concept of JEBAR. Since the JEBAR term is expressed in terms of the interaction between available potential energy of a water column and a bottom slope, the analysis of the energy budget of a seasonal wind-driven circulation may shed light on a further fundamental character of JEBAR. Therefore, we discuss the dynamics of the seasonal variation in the wind-driven ocean circulation in more detail by utilizing the concept of JEBAR.

In Section 4, we clarify the mechanism of reducing the seasonal transport variation in terms of "JEBAR rectification." In Section 5, the fundamental differences between the Kuroshio and the Gulf Stream are discussed together with several mechanisms which are neglected in the present article.

2. Formulation and model description

The basic equations used here are linear, two-layer, planetary geostrophic equations which are derived under the following approximations (Salmon, 1992). First, the phase speed of barotropic planetary waves is assumed to be infinite. This means that the barotropic adjustment is achieved instantaneously. The other approximations are hydrostatic, beta-plane, rigid lid and Boussinesq approximations in a conventional manner. Nonlinear advection is not considered here. With wind forcing and Rayleigh damping, the equations are

$$-fv_1 = -\frac{1}{\rho_0} p_x + \frac{\tau^x}{\rho_0 h_1} - ru_1, \tag{2.1}$$

$$fu_1 = -\frac{1}{\rho_0}p_y + \frac{\tau^y}{\rho_0 h_1} - rv_1, \tag{2.2}$$

$$h_{1t} + (u_1h_1)_x + (v_1h_1)_y = 0 \tag{2.3}$$

for the upper layer denoted by the subscript 1, and

$$-fv_2 = -\frac{1}{\rho_0}p_x + g'h_{1x} - ru_2, \tag{2.4}$$

$$fu_2 = -\frac{1}{\rho_0}p_y + g'h_{1y} - rv_2, \tag{2.5}$$

$$h_{2t} + (u_2h_2)_x + (v_2h_2)_y = 0 \tag{2.6}$$

for the lower layer denoted by the subscript 2. We use the subscripts x, y, t for partial derivatives. The notation is as follows: (x, y, z) are the Cartesian coordinates in the (eastward, northward, upward) directions: (u, v) the (eastward, northward) velocity components; h_i the thickness of the i-th layer; $f = f_0 + \beta_0 y$ the Coriolis parameter; ρ the density; ρ_0 the mean density; $g' = g(\rho_2 - \rho_1)/\rho_0$ the reduced gravity; $p = p(x, y)$ the hydrostatic pressure with which the pressure of each layer is defined as $p_1 = p - \rho_1 gz$ and $p_2 = p - (\rho_2 - \rho_1)gh_1 - \rho_2 gz$, respectively; r the Rayleigh friction coefficient; and (τ^x, τ^y) the surface wind stress components. Those governing equations are used by Salmon (1986) to discuss the steady wind- and thermally driven ocean circulation. In the present article, we focus our attention on seasonal variations. Our major motivation to adopt the planetary geostrophic equations lies in the idea that those equations are simple enough to highlight wind-generated baroclinic activity over bottom topography.

From (2.3) and (2.6), we define the total transport stream function ψ such that

$$u_1h_1 + u_2h_2 = -\psi_y \text{ and } v_1h_1 + v_2h_2 = \psi_x. \tag{2.7}$$

Using the above momentum equations and the relation (2.7), we can obtain each velocity component explicitly. Neglecting r^2 compared with f^2, the results are

$$u_1 = -\frac{1}{H}\psi_y + \frac{1}{f^2}\frac{h_2}{H}\left(-fg'h_{1y} - rg'h_{1x} + \frac{f}{\rho_0 h_1}\tau^y + \frac{r}{\rho_0 h_1}\tau^x\right), \tag{2.8}$$

$$v_1 = \frac{1}{H}\psi_x + \frac{1}{f^2}\frac{h_2}{H}\left(+fg'h_{1x} - rg'h_{1y} - \frac{f}{\rho_0 h_1}\tau^x + \frac{r}{\rho_0 h_1}\tau^y\right), \tag{2.9}$$

$$u_2 = -\frac{1}{H}\psi_y - \frac{1}{f^2}\frac{h_1}{H}\left(-fg'h_{1y} - rg'h_{1x} + \frac{f}{\rho_0 h_1}\tau^y + \frac{r}{\rho_0 h_1}\tau^x\right), \tag{2.10}$$

$$v_2 = \frac{1}{H}\psi_x - \frac{1}{f^2}\frac{h_1}{H}\left(+fg'h_{1x} - rg'h_{1y} - \frac{f}{\rho_0 h_1}\tau^x + \frac{r}{\rho_0 h_1}\tau^y\right), \tag{2.11}$$

where $H = h_1 + h_2$ is the total depth. Adding the upper-layer equations multiplied by h_1 to the lower-layer equations multiplied by h_2 gives

$$-f\nabla\psi = -\frac{1}{\rho_0}H\nabla(p_B - \rho_2 gH) - g'h_1\nabla h_1 + \frac{\boldsymbol{\tau}}{\rho_0} - r\mathbf{k}\times\nabla\psi, \tag{2.12}$$

where $p_B = p + g(\rho_1 h_1 + \rho_2 h_2)$ is the bottom pressure (where the subscript B denotes the bottom) and $\mathbf{k}$ is the vertical unit vector. Eq. (2.12) corresponds to the vertically integrated equation of motion without bottom friction, but mathematically the last term on the right-hand side plays a similar role to the Ekman bottom friction which may establish Stommel-type western boundary layers. Dividing (2.12) by H and taking the curl afterwards, we find the diagnostic vorticity equation

$$J\left(\psi, \frac{f}{H}\right) = J\left(\frac{g'}{2}h_1^2, \frac{1}{H}\right) + \frac{1}{\rho_0}\operatorname{curl}\frac{\boldsymbol{\tau}}{H} - r\nabla\cdot\left(\frac{1}{H}\nabla\psi\right), \tag{2.13}$$

where J denotes the Jacobian. Substitution of (2.8) and (2.9) into (2.3) yields the prognostic h-equation

$$h_{1t} + J\left(\psi, \frac{h_1}{H}\right) + J\left(g'h_1, \frac{h_1h_2}{fH}\right) - \nabla\cdot\left(\frac{rg'h_1h_2}{f^2H}\nabla h_1\right) + \operatorname{curl}\left(\frac{h_2}{\rho_0 fH}\boldsymbol{\tau}\right) + \nabla\cdot\left(\frac{rh_2}{\rho_0 f^2 H}\boldsymbol{\tau}\right) = 0. \tag{2.14}$$

For the sake of later parameter studies, we nondimensionalize the above two equations using characteristic scales L, D, U, c_0, f_0 and τ_0 as follows:

$$(x, y) \to L(x, y), \qquad (H, h_1) \to D(H, h), \qquad (u, v) \to U(u, v),$$
$$t \to (L/c_0)t, \qquad \psi \to DLU\psi, \quad f \to f_0 f, \qquad \boldsymbol{\tau} \to \tau_0\boldsymbol{\tau}.$$

In particular, L is the basin size, D is the total depth in the flat-bottom interior, and U is the horizontal velocity scale. In order to distinguish the time scale of the wave propagation from that of the advection, we have introduced another velocity scale c_0 which is the typical phase speed of baroclinic long planetary waves given by

$$c_0 = \beta_0\frac{g'D_1D_2}{f_0^2 D}, \tag{2.15}$$

where D_i is the characteristic constant depth of the i-th layer. The resulting

nondimensional forms for (2.13) and (2.14) are

$$J\left(\psi, \frac{f}{H}\right) = \frac{1}{\omega FM} J\left(\frac{h^2}{2}, \frac{1}{H}\right) + \tau \operatorname{curl} \frac{\boldsymbol{\tau}}{H} - \epsilon \nabla \cdot \left(\frac{1}{H} \nabla \psi\right) \tag{2.16}$$

and

$$\begin{aligned} h_t + MJ\left(\psi, \frac{h}{H}\right) + \frac{1}{\omega F} J\left(h, \frac{h}{f}\left(1 - \frac{h}{H}\right)\right) - \frac{\epsilon}{\omega F} \nabla \cdot \left(\frac{h}{f^2}\left(1 - \frac{h}{H}\right) \Delta h\right) \\ + \tau M \operatorname{curl}\left(\frac{1}{f}\left(1 - \frac{h}{H}\right)\boldsymbol{\tau}\right) + \epsilon \tau M \nabla \cdot \left(\frac{1}{f^2}\left(1 - \frac{h}{H}\right)\boldsymbol{\tau}\right) = 0, \end{aligned} \tag{2.17}$$

respectively where $f = 1 + \beta y$ and the nondimensional parameters are defined by $\beta = \beta_0 L / f_0$ (beta parameter), $\omega = c_0/(f_0 L)$, $M = U/c_0$ (planetary "Mach" number), $F = f_0^2 L^2/(g'D)$ (internal rotational Froude number), $\epsilon = r/f_0$ and $\tau = \tau_0/(\rho_0 f_0 DU)$, respectively. The vorticity equation (2.16) is linear in ψ. Hence, it is convenient to divide the total transport *a posteriori* into the JEBAR part driven by the first term on the right-hand side of (2.16) and the wind-driven part due to the second term of the same equation (see Greatbatch *et al.*, 1991):

$$\psi = \psi_{\text{JEBAR}} + \psi_{\text{WIND}}.$$

These expressions will be used in the later sections.

The boundary condition is that the normal component of velocity vanishes at the coast. Thus, the boundary condition imposed on ψ should be ψ = constant but we may choose this constant at zero without losing generality, viz,

$$\psi = 0. \tag{2.18}$$

On the other hand, the boundary condition on h can be derived from (2.8)–(2.11) with (2.18). Thus, we impose (in nondimensional form)

$$hh_y = -\frac{\epsilon}{f} hh_x + \omega \tau FM\left(\tau^y + \frac{\epsilon}{f}\tau^x\right) \tag{2.19}$$

along meridional boundaries, and

$$hh_x = \frac{\epsilon}{f} hh_y + \omega \tau FM\left(\tau^x - \frac{\epsilon}{f}\tau^y\right) \tag{2.20}$$

along zonal boundaries, respectively.

The governing equations (2.16) and (2.17) together with the boundary conditions (2.18), (2.19) and (2.20) comprise a well-posed system: the velocity field is deter-

mined by (2.16) *diagnostically,* but it changes through the variation of the interface (i.e., h-field) in which the wind variation is reflected by (2.17).

The model ocean is basically similar to that of Stommel (1948) except for variable bottom topography. The experiment is performed in a square basin on $0 \leq x \leq 1$, $-0.5 \leq y \leq 0.5$. The characteristic parameters are taken as $L = 2000$ km, $D = 4000$ m, $f_0 = 7.3 \times 10^{-5}$ s^{-1} (i.e., the reference latitude is located at 30N), $\beta_0 = 2 \times 10^{-11}$ m^{-1} s^{-1} and $U = 1.2 \times 10^{-3}$ m s^{-1} corresponding to the Sverdrup speed for the wind stress variation of 0.1 N m^{-2} over half of the entire basin, $g' = 0.02$ m s^{-2} and $\rho_0 = 1035$ kg m^{-3}. The ratio of the upper layer depth to the total depth is 0.15 at the initial state (i.e., $D_1/D = 0.15$). From (2.15), we therefore obtain $c_0 = 3.8 \times 10^{-2}$ m s^{-1}.

The total depth for the control experiment is given by the form

$$H = a + (1 - a) \tanh b(x - 0.2), \tag{2.21}$$

that is, the continental slope is located on the western side of the basin, and an approximately flat domain having the depth of unity extends to the eastern boundary. Another form is given by

$$H = a + (1 - a) \tanh b(0.3 - y), \tag{2.22}$$

that is, the continental slope is located at the northern side. This is to examine the effect of the meridional gradient of the slope because the actual continental slope off the south coast of Japan is oblique. For both cases, we vary values of a and b to change the height and the gradient of the slope, respectively, while the location at which the gradient of the slope becomes maximum is fixed. For the case of the western continental slope, three combinations of (a, b) are chosen as (0.64, 8.33), (0.72, 5) and (0.81, 3.57); the intermediate case is referred to as "standard slope" hereafter (Fig. 2). On the other hand, only the standard slope is adopted for the case of the northern continental slope because results are easily generalized. The wind stress applied here has only a zonal component such that $\tau^x = \sin \pi y$ and $\tau^y = 0$ just for simplicity. However, we will introduce time-dependence in some experiments. The nondimensional parameters are $\beta = 0.55$, $\omega = 2.6 \times 10^{-4}$, $M = 0.032$, $F = 266$, $\epsilon = 0.01$ and $\tau = 0.1$. These parameters are deliberately chosen in order to avoid both outcropping of the lower layer and intersection of the interface with the continental slope (cf. Salmon, 1994).

We solve the simultaneous equations (2.16) and (2.17) numerically with 101×101 grid points. In some complementary cases with small friction, the resolution is increased to 201×201 grid points. The stream function ψ and the upper-layer thickness h is obtained as follows. Adopting the leapfrog scheme with the Euler-backward or Matsuno scheme done every 20 steps, time integration of (2.17) is conducted with the use of the latest ψ. The stream function ψ is then solved by using

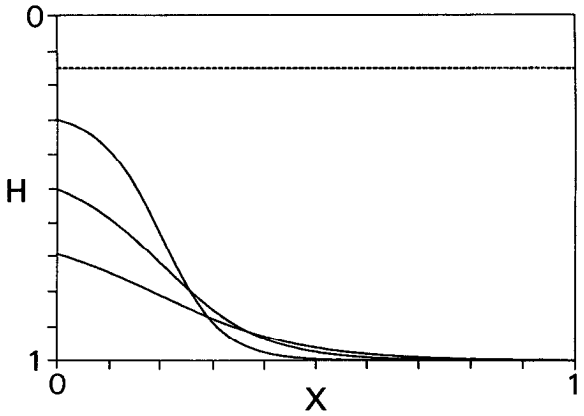

Figure 2. Three cases of the western continental slope. The intermediate case corresponds to the standard slope. The dotted line denotes the interface at rest.

(2.16) with the resulting h at each time step using the sequential over-relaxation (SOR) method. Our simulation is carried out in the following way. First, we spin up to a steady state from rest with keeping the wind steady, as discussed in Section 3. Then, by switching the steady wind to the seasonal wind, the seasonal variation in the model circulation is investigated in Section 4.

3. The steady state

As pointed out by Veronis (1973) and confirmed numerically by Anderson and Killworth (1977), the steady state of our model ocean must be the same as that of the nontopographic ocean. This is because the wind stress acts only on the upper layer like a body force in our model and no mechanisms that generate steady currents in the immiscible lower layer exist (cf. Rooth *et al.*, 1978). We prove this classical result analytically, particularly emphasizing the role of JEBAR, and then demonstrate it numerically.

a. Analytical verification. Using (2.14), after neglecting the time-derivative term, we obtain an expression for the JEBAR term in dimensional form:

$$J\left(\frac{g'}{2}h_1^2, \frac{1}{H}\right) = \frac{f}{h_2}\left[J\left(\psi, \frac{h_2}{H}\right) - \frac{1}{H}J\left(g'h_1, \frac{h_1h_2}{f}\right) + \nabla\cdot\left(\frac{rg'h_1h_2}{f^2H}\nabla h_1\right) - \mathrm{curl}\left(\frac{h_2}{f\rho_0 H}\boldsymbol{\tau}\right) - \nabla\cdot\left(\frac{rh_2}{f^2\rho_0 H}\boldsymbol{\tau}\right)\right]. \tag{3.1}$$

Substituting (3.1) into the vorticity equation (2.13) yields another form of the

governing equation

$$\frac{f}{Hh_2}\mathbf{k}\cdot\left(-f\nabla\psi + g'h_1\nabla h_1 - \frac{\boldsymbol{\tau}}{\rho_0}\right)\times\nabla\frac{h_2}{f}$$
$$= r\left\{\nabla\cdot\left[\frac{1}{fH}\left(-f\nabla\psi + g'h_1\nabla h_1 - \frac{\boldsymbol{\tau}}{\rho_0}\right)\right]\right. \tag{3.2}$$
$$\left. - \frac{1}{Hh_2}\nabla\frac{h_2}{f}\cdot\left(g'h_1\nabla h_1 - \frac{\boldsymbol{\tau}}{\rho_0}\right)\right\}.$$

Away from the coastal boundary layer, we may neglect the friction terms. Thus, the interior flow is a solution to

$$\mathbf{k}\cdot\left(-f\nabla\psi + g'h_1\nabla h_1 - \frac{\boldsymbol{\tau}}{\rho_0}\right)\times\nabla\frac{h_2}{f} = 0. \tag{3.3}$$

This equation is identically satisfied if

$$-f\nabla\psi + g'h_1\nabla h_1 - \frac{\boldsymbol{\tau}}{\rho_0} = \nabla G\left(\frac{h_2}{f}\right), \tag{3.4}$$

where G is an arbitrary function of h_2/f. Hence, comparing this equation with (2.12), it is found that the bottom pressure term

$$-\frac{1}{\rho_0}H\nabla(p_B - \rho_2 gH)$$

is *irrotational.* That is, the bottom pressure torque

$$\frac{1}{\rho_0}J(p_B, H) \tag{3.5}$$

must vanish in the steady state. On the other hand, the curl of (3.4) leads to

$$J(\psi, f) = \frac{1}{\rho_0}\operatorname{curl}\boldsymbol{\tau}. \tag{3.6}$$

Therefore, outside the boundary layer, the steady flow proves to be exactly the nontopographic Sverdrup flow as expected.

An alternative expression for the JEBAR term can be derived straightforwardly from (3.1), namely,

$$J\left(\frac{g'}{2}h_1^2, \frac{1}{H}\right) = fJ\left(\psi, \frac{1}{H}\right) - \frac{1}{\rho_0}(\mathbf{k}\times\boldsymbol{\tau})\cdot\nabla\frac{1}{H}$$
$$+ \frac{f}{Hh_2}\operatorname{curl}\left[\frac{h_2}{f}\left(-f\nabla\psi + \nabla\frac{g'}{2}h_1^2 - \frac{\boldsymbol{\tau}}{\rho_0}\right)\right]. \tag{3.7}$$

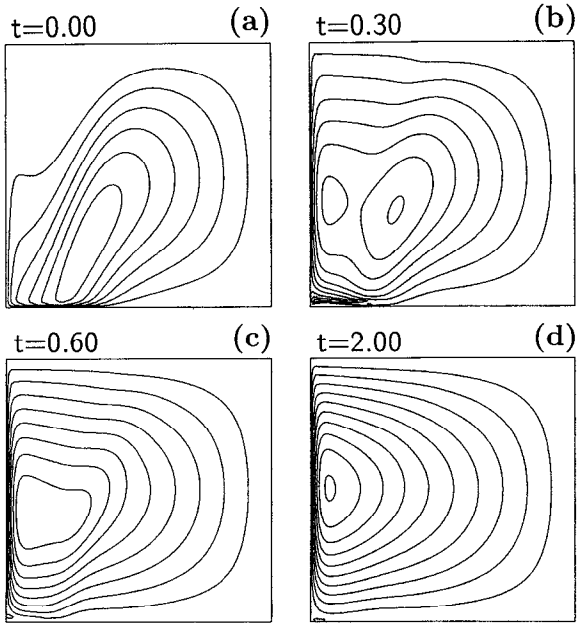

Figure 3. Stream function ψ at four different stages of the spin-up experiment for the case of the standard slope. The zonal wind stress is given by $\tau^x = \sin \pi y$. The contour interval is 0.05. The nondimensional time unity corresponds to 1.67 years. The region of negative values is shaded. The nondimensional parameters are $\beta = 0.55$, $\omega = 2.6 \times 10^{-4}$, $M = 0.032$, $F = 266$, $\epsilon = 0.01$ and $\tau = 0.1$.

The last term on the right-hand side is zero because of (3.4). Thus, (3.7) reduces to

$$J\left(\frac{g'}{2}h_1^2, \frac{1}{H}\right) = -\frac{1}{H^2}\left(f\mathbf{k} \times \nabla\psi + \frac{1}{\rho_0}\mathbf{k} \times \boldsymbol{\tau}\right) \cdot \nabla H, \tag{3.8}$$

which is in agreement with the result obtained directly from the two vorticity equations (2.13) and (3.6). It is clear that JEBAR plays a fundamental role in compensating the topographic vortex-stretching due to both the barotropic and the Ekman flows. Note that the above result is consistent with Mertz and Wright (1992) who discuss the case of continuous stratification.

b. Numerical results. The numerical solutions to (2.16) and (2.17) for the western continental slope are shown in Figure 3. This demonstrates spin-up processes from rest. The wind whose meridional profile is given by $\tau^x = \sin \pi y$ and $\tau^y = 0$ is turned on at $t = 0$ and thereafter kept constant. A flow field, corresponding to the steady flow in homogeneous fluid, is generated instantaneously at $t = 0$ (Fig. 3a). This is because the phase speed of the barotropic Rossby waves is assumed infinite in our model. This initial circulation is composed of the slope current along the f/H contours, the

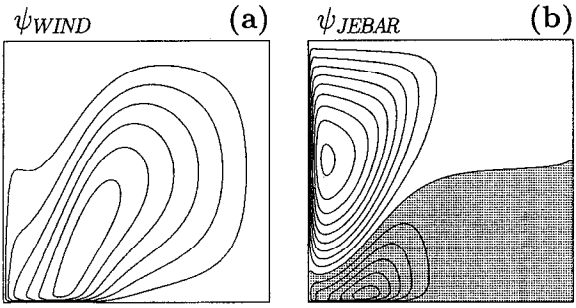

Figure 4. Steady-state stream function ψ_{WIND} (left) and ψ_{JEBAR} (right) contributed by the wind and JEBAR forcing, respectively. The western continental slope and the nondimensional parameters are the same as in Figure 3. The contour interval is 0.05. The region of negative values is shaded.

interior Sverdrup flow, and the frictional southern boundary layer due to the topographic beta-effect; a detailed physical explanation is given by Salmon (1992). The total transport of the initial flow is less than the nontopographic Sverdrup transport simply due to the topographic beta-effect for the barotropic flow (Schulman and Niiler, 1970). This homogeneous flow is weakened with increasing the steepness of the bottom slope since the topographic beta increases.

As time elapses, the flow in the lower layer becomes rapidly compensated (Figs. 3b–3d). In fact, an almost steady-state flow pattern, i.e., the Sverdrup interior plus the Stommel-type western boundary current can be seen after the baroclinic long Rossby waves propagate across the entire basin. It is confirmed that the same Sverdrup balance is achieved for any bottom topography submerged in the lower layer and that the transport increases up to the nontopographic Sverdrup transport $\pi\tau/\beta$ (estimated at the reference latitude) with the error of $O(\epsilon/\beta)$ (i.e., the width of the frictional western boundary layer) as time elapses. The steady-state flow minus the initial flow is shown in Figure 4. The difference corresponds to the *compensation* part or the JEBAR part ψ_{JEBAR} defined in Section 2 (Fig. 4b); the initial flow corresponds to the wind-driven part ψ_{WIND} (Fig. 4a). We note that the western boundary current is composed mainly by ψ_{JEBAR} over the western continental slope. Another important aspect of ψ_{JEBAR} is that the southern boundary currents due to ψ_{WIND} is canceled by the JEBAR-induced cyclonic gyre at the southern part of the slope region in Figure 4b. The existence of the cyclonic gyre is easily understood by the simple vorticity argument as follows. Since ∇H directs eastward, nonzero h_y is required to generate the JEBAR forcing in (2.16). The upper layer (h-field; not shown here) is the deepest at the reference latitude where the stream function shows its maximum and shoals toward the zonal boundaries due to the Ekman pumping. That is, $h_y < 0$ ($h_y > 0$) in the northern (southern) half of the basin. Therefore, the JEBAR term in (2.16) is negative in the northern part of the slope region, whereas it is positive and opposite to the wind stress curl in the southern part. The latter

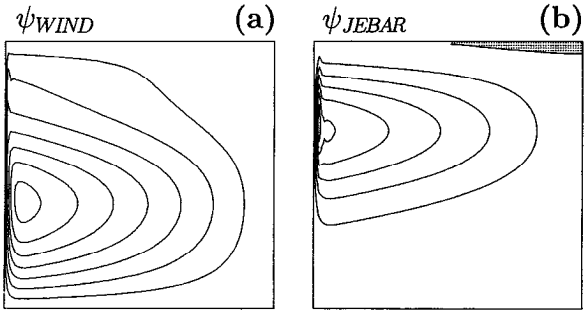

Figure 5. As in Figure 4 but for the case of the northern continental slope given by $H = 0.72 + 0.28 \tanh 5(0.3 - y)$.

introduces the positive vorticity that is needed to generate the cyclonic gyre. In the case of the northern continental slope, on the other hand, ψ_{JEBAR} shows only an anticyclonic gyre (Fig. 5). In the latter case, only h_x is capable of producing the JEBAR forcing since ∇H directs southward. Considering the fact that h_x is negative everywhere in the northern slope region away from the western boundary layer, the JEBAR forcing has the same negative sign as the wind stress curl.

Since the JEBAR part is determined explicitly by the density structure, it is less sensitive to temporal changes of winds. This aspect of the JEBAR forcing is also recognized by Huthnance (1984) who investigates the persistence of the eastern boundary currents over the continental slopes under the observed horizontal density gradient. The wind-driven circulation may be affected by the JEBAR forcing only when the baroclinic long Rossby waves propagate to modify the density structure. In other words, it is expected that the JEBAR-induced transport, with releasing the available potential energy accumulated by the wind action, makes the total transport less sensitive to rapid changes of the winds by a kind of rectification. In particular, this is the case for the western continental slope, in which the JEBAR-induced transport is comparable to or dominates the transport of the western boundary current (Fig. 4b). The next section discusses more details of the above process to understand seasonal transport variations of the Kuroshio.

We note here that slight disturbances are seen at the southwest corner in Figure 3 and near the western boundary in Figure 5 in the steady state. It is possibly due to insufficient resolution of our numerical scheme for the thin boundary layers there. We believe, however, that the interior of our model ocean is not affected by this boundary layer because no nonlinear advection is included in our model. In addition, the displacement of the interface is so small in the present model that the geostrophic contours originated from the western boundary never return to the same boundary. Thus, the situation is not the case cautioned by Ierley and Young (1983). Therefore, no measures are taken to smear out the disturbance in the present experiment.

4. Seasonal variations

In this section, we examine the response of our model ocean to seasonally varying winds. We simplify the seasonal variation in the wind stress in the northwestern Pacific by considering overall features revealed in the Hellerman and Rosenstein's (1983) monthly climatological data. Again, only the zonal stress is applied (i.e., $\tau^y = 0$) to (2.17) with its sinusoidal variation both in time and space, namely,

$$\tau^x = A(t) \sin \pi y \text{ and } A(t) = 0.75 \sin 2\pi\sigma t + 1, \tag{4.1}$$

where $\sigma = 1/(1 \text{ year})$ or 1.67 in dimensionless unit. Indeed, it is highly idealized but the most principal features are retained in an exaggerated way. The steady state obtained in the previous section is used as the initial value of (2.17). It turns out that the response to the wind variation becomes periodic rather quickly for all cases presented here.

a. The western continental slope. Figure 6 shows the time variations in the simulated northward transport for the three different slopes (see Fig. 2) along the western boundary, the nontopographic Sverdrup transport $\pi\tau A(t)/\beta$, the topographic Sverdrup transport (i.e., the transport for a single-layer model with the same topography), and the available potential energy defined by

$$\int\int \frac{\eta^2}{2} dxdy, \tag{4.2}$$

where $\eta = h - D_1/D$ is the (nondimensional) displacement of the interface (note again that $\eta \ll D_1/D$ in the present experiment). The area integration of (4.2) is done over the whole basin. Figure 6 also shows the changes in the maxima of ψ_{JEBAR} and ψ_{WIND} defined in the previous section.[2]

It is seen clearly that the amplitude of the seasonal variation in the simulated total transport is roughly one third of that associated with the nontopographic Sverdrup transport. Since $|H_x| \gg |h_y|$ in our model, the JEBAR term increases as the gradient of the slope increases even if the width of the slope region is reduced. In addition, as the slope becomes steeper, the topographic beta-effect becomes more important. Thus, the seasonal variation must weaken as the gradient of the slope increases. The minimum transport in all cases, however, is much greater than that of the nontopographic Sverdrup transport. This rectification is a consequence of JEBAR as we have indicated in the previous section. We note that the total available potential energy increases in winter when the winds are strong. This is simply because the Ekman pumping is the most active in winter.

2. The sum of the peaks of each component is not equal to the maximum of ψ which corresponds to the total transport of the western boundary current because their locations change. In particular, ψ_{WIND} contributes little to the western boundary current in summer as we will see in the text.

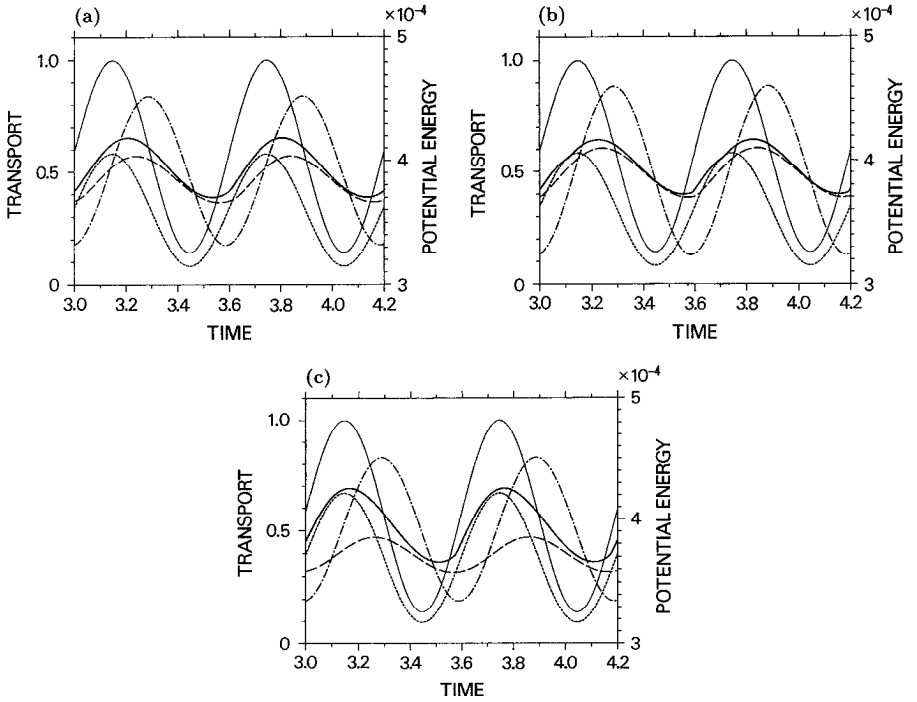

Figure 6. Seasonal variation of the total transport for the standard slope (a), for the steep slope (b) and for the mild slope (c). The total transport along the western boundary of the present simulation is denoted by the thick solid line; the nontopographic Sverdrup transport is denoted by the thin solid line; the JEBAR part ψ_{JEBAR} is denoted by the dashed line; the topographic Sverdrup transport ψ_{WIND} is denoted by the dotted line. The available potential energy is also shown by the dot-dash line. The period of the wind oscillation is 1 year (0.6 in nondimensional unit).

Figure 7 shows the horizontal patterns of the stream function at different phases of the seasonal cycle for the case of the standard slope. Each phase roughly corresponds to four different seasons. We find the well-defined double-gyre structure composed of the perpetual, large anticyclonic gyre in the main part of the slope region and the small southern cyclonic gyre only during the summer season of weak wind forcing (Fig. 7d). The former anticyclonic circulation is mostly driven by the JEBAR forcing when the winds are weak (see Fig. 6). This is consistent with another feature that the stream function shows two peaks when the wind is strong (e.g., Fig. 7a). The interior wind-generated barotropic flow cannot enter the western slope region due to the familiar effect of "blocking" by the bottom slope but JEBAR continues to force the anticyclonic circulation over the slope region. The southern cyclonic gyre seen in Fig. 7d exists because the sign of the vorticity generated by the JEBAR forcing is opposite to the wind stress curl as discussed in Section 3b. Thus, the coupling of the bottom topography and the density structure releases the available potential energy

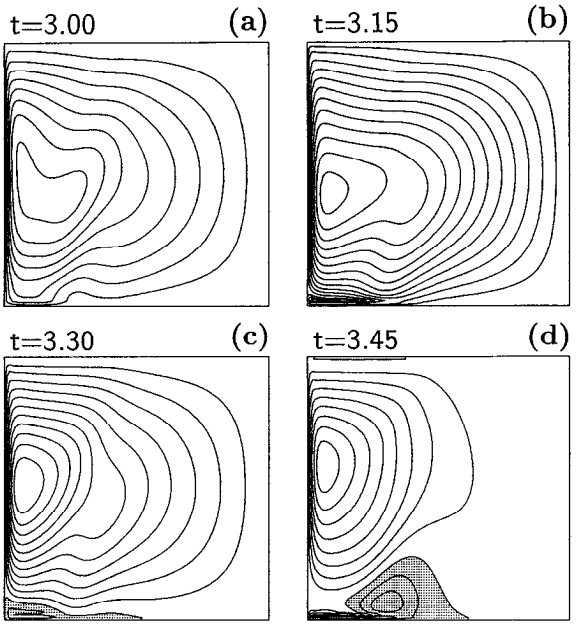

Figure 7. Stream function ψ corresponding to Figure 6a. The contour interval is 0.05. The region of negative values is shaded. (a) Autumn. (b) Winter. (c) Spring. (d) Summer.

periodically (Fig. 6) and mitigates the influence of the strong seasonality of winds. Actually, the total available potential energy decreases rapidly in summer (see Fig. 6), suggesting the active energy conversion into the kinetic energy. This mechanism may be called "JEBAR rectification." Figure 8, which shows the seasonal variation in ψ_{JEBAR} field, demonstrates clearly this property of the JEBAR forcing.

The present model configuration is much different from reality. In particular, the continental slope region occupies a large area of the whole basin as shown in Figure 2. However, we expect that the unique role of JEBAR described above becomes even more prominent as the zonal extent of the basin increases. Even if the Sverdrup transport increases with the zonal extent, the recirculation over the slope is much more strengthened because the JEBAR forcing is related to the square of the interface displacement which is determined basically by the basinwide structure (see (2.13)). An additional experiment, in which the zonal extent of a basin is doubled, confirms this tendency. Figures 9 and 10 demonstrate clearly that the transport of the western boundary current is almost perfectly determined by the JEBAR forcing in summer and by the topographic Sverdrup balance in winter.

The Rayleigh-type damping terms in (2.16) and (2.17) may affect the phase of the transport variation. The damping time adopted here is $r^{-1} = 16$ days. This friction coefficient ($\epsilon = 0.01$ in nondimensional unit) seems to be much larger than a plausible value. However, the result of Figure 6 suggests that the friction terms in

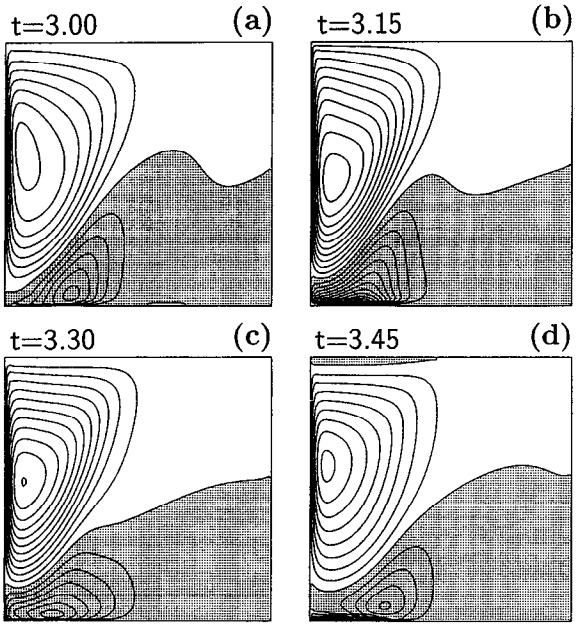

Figure 8. As in Figure 7 but for the JEBAR part ψ_{JEBAR}. The contour interval is 0.05. The region of negative values is shaded.

(2.16) and (2.17) do not affect the wave propagation. The reason lies in the fact that the damping has the form of Rayleigh friction, that is, the dissipation is assumed only in the momentum equations but not in the continuity equation. This type of friction is less effective in damping baroclinic waves (Yamagata and Philander, 1985; see also

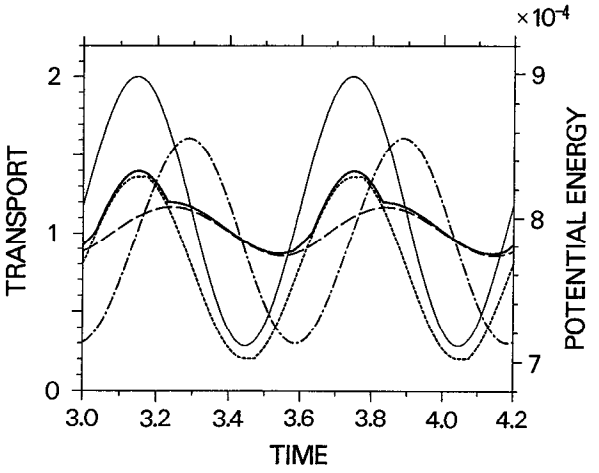

Figure 9. As in Figure 6b but for a basin of doubled zonal extent. The available potential energy here is area-averaged.

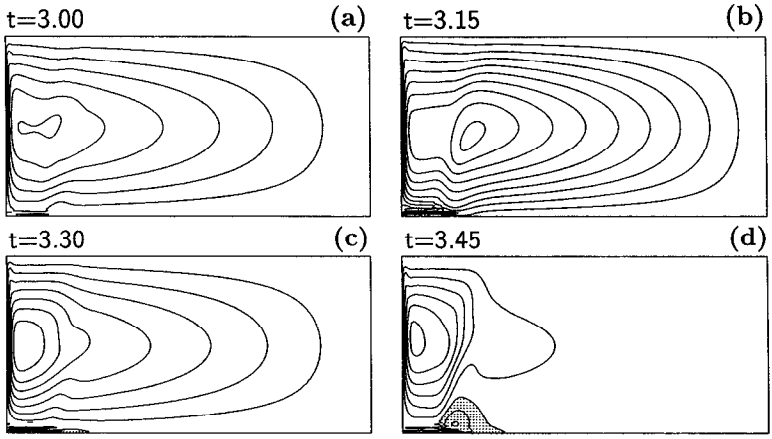

Figure 10. Stream function ψ corresponding to Figure 9. The contour interval is 0.15. The region of negative values is shaded.

Anderson and Killworth, 1979). In fact, a complementary experiment with $\epsilon = 0.004$ ($r^{-1} = 40$ days) confirms this (not shown) and the phase property is approximately the same as that in the case of $\epsilon = 0.01$.

b. The northern continental slope. The result in the case of the northern continental slope is essentially similar to that in the case of the western continental slope (Fig. 11). That is, the seasonal variation in the total transport is reduced due to the "JEBAR rectification" discussed above. However, we observe some new features which should be described here (Figs. 11 and 12).

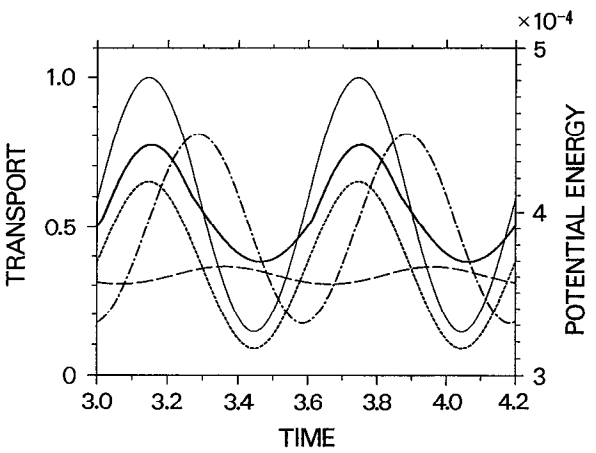

Figure 11. As in Figure 6 but for the case of the northern continental slope given by $H = 0.72 + 0.28 \tanh 5(0.3 - y)$.

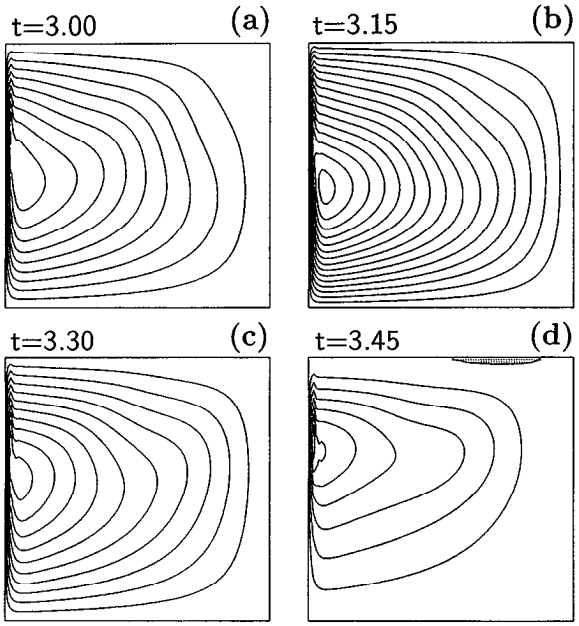

Figure 12. As in Figure 7 but for the case of the northern continental slope.

Since the topographic "blocking" takes place over the northern slope, the total transport variation of the western boundary current is more affected by the wind changes (see Fig. 5). In addition, h_x is much smaller than h_y. Therefore, the JEBAR part of the transport is quite small in the present case; it is overwhelmed by the wind-driven part. This is why the total transport changes more in phase as a whole with the Sverdrup transport than that for the case of the western continental slope.

The anticyclonic subtropical gyre can be separated spatially into ψ_{JEBAR} and ψ_{WIND} contributions, as seen in Figure 5. Since these components respond differently to the seasonal winds, the western boundary current is dominated by ψ_{JEBAR} in the northern half of the basin and by ψ_{WIND} in the southern half, respectively. Therefore, when we discuss the transport variations, it is important to notice the location of the section across which the transport is measured (Fig. 12). Actually, the curve for the JEBAR-induced part in Figure 11 corresponds to the seasonal variation in the western boundary current measured across the section located in the northern half of the basin. This is in contrast to the case of the western continental slope, in which the total transport of the western boundary current is always dominated by the JEBAR-induced part.

Finally, we note here that the amplitude of the seasonal variations as well as the mean value itself of the JEBAR contribution is much smaller than that in the case of the western continental slope (Figs. 6 and 11). This is reasonable because the zonal gradient of h is basically small over the slope as mentioned above. Furthermore, the

seasonal variation in the JEBAR contribution reflects that of h_x in the present case (Fig. 11) rather than h_y in the case of the western continental slope (Fig. 6). It is also interesting to note that the transport variation across the PN-line (see Fig. 1) looks quite similar to the ψ_{JEBAR} contribution in Figure 11. Although it is difficult to identify the location of the PN-line in the present simple model configuration, the correspondence appears to be more than fortuitous.

5. Summary and discussion

We are successful in explaining the main subject of the present article, i.e., the reduction of the seasonal variation in the total transport observed for the Kuroshio (and the Florida Current as well), in terms of JEBAR. The relatively rich model transport compared with the small nontopographic Sverdrup transport in summer is provided by the barotropic flow generated by the interaction between the baroclinicity and the bottom topography, i.e., by the JEBAR forcing in a narrow sense. It is this process that has been missed in the previous studies. The reduction of the transport compared with the nontopographic Sverdrup transport in winter is simply attributable to the topographic beta-effect due to vortex-shrinking on the slope; the mechanism of this phase is essentially barotropic and demonstrated clearly in Anderson and Corry (1985b). From the energetic point of view, as suggested by Holland (1975), the available potential energy is released by the JEBAR forcing in (2.13) to produce the barotropic flow when the winds are weak in summer. On the other hand, when the winds are strong, the barotropic flow excited by the wind forcing impinges on the bottom slope to induce the baroclinic mode. This role is played by the second term of (2.14). As is well-known, the baroclinic waves are also excited directly by the wind action. This role is played by the fifth term of (2.14). Thus, the wind forcing accumulates the available potential energy.

The location of the continental slope affects the spatial distributions of ψ_{JEBAR} and ψ_{WIND} and hence determines the relative importance between the directly wind-induced transport and the JEBAR-induced transport. For the case of the western continental slope, the total transport of the western boundary current is governed mainly by the JEBAR-induced part and is less sensitive to the wind variations. On the other hand, for the case of the northern continental slope, the western boundary current itself changes its characters in the meridional direction; it is directly controlled by the winds in the south but dominated by the JEBAR-induced part in the north. The actual situation surrounding the Kuroshio region is such that the Asian Continent is located to the west of the basin and the Japan Islands to the north, with corresponding continental slopes. Thus, we conclude that the seasonal transport variation of the Kuroshio is expected to be severely controlled by the JEBAR forcing.

The observed 180° out of phase relation between the transport of the Kuroshio and the Sverdrup transport cannot be explained completely by the present simple model.

However, the JEBAR-driven component for the case of the northern continental slope shows such a tendency. Therefore, we suggest that a rather realistic continental slope may explain the observed transport variation across the PN-line, at least qualitatively. As implied by Veronis (1981), the barotropic and/or baroclinic instability over the continental slope, together with the "Neptune effect" (Holloway, 1992), may also explain the observed phase lag. We have neglected these interesting mesoscale processes in the present simple model. However, a recent experiment using a high-resolution ocean general circulation model with the σ-coordinate supports the above expectation (see Fig. 1).

The model ocean used here is purely wind-driven, so that the modification of the transport by JEBAR is determined internally; the total transport never exceeds the nontopographic Sverdrup transport. The present picture seems to be generally in accord with a common view on the seasonal variation in the Kuroshio transport. However, in contrast with the case of the Kuroshio, buoyancy-driven thermohaline processes cannot be neglected for its North Atlantic counterpart, since it is well known that the transport of the Gulf Stream is larger than Sverdrup transport. Even so, the basic role of JEBAR clarified here seems to be important for explaining the seasonal transport changes of two major western boundary currents in the northern hemisphere (cf. Anderson and Corry, 1985a; 1985b).

Acknowledgments. The authors are grateful to Dr. D. L. T. Anderson for providing helpful information especially on his earlier works on the seasonal variation in the Florida Current and Dr. R. J. Greatbatch for encouraging communication on the concept of JEBAR. The present work is supported by the International Scientific Research Program (No. 05044034) from the Japan Ministry of Education, Science and Culture (JMESC). The work is also a contribution to the Basic Research Program for the Global Ocean Observing System under JMESC.

APPENDIX

A multi-layer formulation of the JEBAR term

We derive here the N-layer expression for the JEBAR term. Suppose that we integrate vertically the equation of motion

$$f\mathbf{k} \times \mathbf{v} = -\frac{1}{\rho_0}\nabla p + \frac{\boldsymbol{\tau}}{\rho_0} - r\mathbf{v} \tag{A1}$$

instead of the two-layer shallow water equations in Section 2. All terms except for the pressure term are readily represented by using the stream function ψ and the surface wind stress. The vertically integrated pressure term is calculated as

$$-\frac{1}{\rho_0}\int_{-H}^{0} p_x dz = -\frac{1}{\rho_0} p_{Bx} H - \frac{1}{\rho_0}\frac{\partial}{\partial x}\int_{-H}^{0} zg\rho dz, \tag{A2}$$

$$= -\frac{1}{\rho_0} p_{Bx} H - \frac{g}{\rho_0} \int_{-H}^{0} z\rho_x dz + \frac{g}{\rho_0} \rho_B H H_x, \tag{A3}$$

in the same notation as Section 2. Thus far, the above formula is applicable to a continuously stratified case (in particular, the expression of (A2) is familiar). For the two-layer model, the second term in (A3) may be reduced to

$$-\frac{g}{\rho_0} \int_{-H}^{0} z\rho_x dz = -\frac{g}{\rho_0} \left[\int_{-h_1-\epsilon}^{-h_1+\epsilon} z\rho_x dz \right]_{\epsilon \to 0} = -\frac{\rho_2 - \rho_1}{\rho_0} g h_1 h_{1x} \equiv -\chi_x, \tag{A4}$$

where

$$\chi \equiv \frac{g'}{2} h_1^2 \tag{A5}$$

is the potential energy in the two-layer system. Thus, (2.12) is again obtained.

The above formulation, although not very straightforward, has an advantage in that it can be easily extended to the N-layer model since merely the number of immiscible interface is increased. Thus, the potential energy and the JEBAR term in the N-layer model are readily found as

$$\chi^{(N)} = \sum_{i=1}^{N-1} \frac{g^{(i)}}{2} H_i^2 - \frac{g\rho_N}{2\rho_0} H^2 \tag{A6}$$

and

$$J\left(\chi^{(N)}, \frac{1}{H}\right) = \sum_{i=1}^{N-1} J\left(\frac{g^{(i)}}{2} H_i^2, \frac{1}{H}\right), \tag{A7}$$

respectively, where ρ_i is the density of the i-th layer, H_i denotes the depth of the i-th interface, and

$$g^{(i)} \equiv \frac{\rho_{i+1} - \rho_i}{\rho_0} g \tag{A8}$$

is the i-th reduced gravity.

REFERENCES

Anderson, D. L. T. and R. A. Corry. 1985a. Ocean response to low frequency wind forcing with application to the seasonal variation in the Florida Straits-Gulf Stream. Prog. Oceanogr., *14,* 7–40.

—— 1985b. Seasonal transport variations in the Florida Straits: A model study. J. Phys. Oceanogr., *15,* 773–786.

Anderson, D. L. T. and P. D. Killworth. 1977. Spin-up of a stratified ocean, with topography. Deep-Sea Res., *24,* 709–732.

—— 1979. Non-linear propagation of long Rossby waves. Deep-Sea Res., *26,* 1033–1050.

Gates, W. L. 1966. On the dynamical formulation of the large-scale momentum exchange between atmosphere and ocean. J. Mar. Res., *24,* 105–112.

Greatbatch, R. J., A. F. Fanning, A. D. Goulding and S. Levitus. 1991. A diagnosis of interpentadal circulation changes in the North Atlantic. J. Geophys. Res., *96,* 22009–22023.

Hellerman, S. and M. Rosenstein. 1983. Normal monthly wind stress over the world ocean with error estimates. J. Phys. Oceanogr., *13,* 1093–1104.

Hidaka, K. 1949. Mass transport in ocean currents and lateral mixing. J. Mar. Res., *8,* 132–136.

Holland, W. R. 1973. Baroclinic and topographic influences on the transport in western boundary currents. Geophys. Fluid Dyn., *4,* 187–210.

—— 1975. Energetics of baroclinic oceans, *in* Numerical Models of Ocean Circulation, National Academy of Sciences, Washington, D. C., 364 pp.

Holland, W. R. and A. D. Hirschman. 1972. A numerical calculation of the circulation in the North Atlantic Ocean. J. Phys. Oceanogr., *2,* 336–354.

Holloway, G. 1992. Representing topographic stress for large-scale ocean models. J. Phys. Oceanogr., *22,* 1033–1046.

Huthnance, J. M. 1984. Slope currents and "JEBAR". J. Phys. Oceanogr., *14,* 795–810.

Ierley, G. R. and W. R. Young. 1983. Can the western boundary layer affect the potential vorticity distribution in the Sverdrup interior of a wind gyre? J. Phys. Oceanogr., *13,* 1753–1763.

Luyten, J. R., J. Pedlosky and H. Stommel. 1983. The ventilated thermocline. J. Phys. Oceanogr., *13,* 292–309.

McCreary, J. P. 1981. A linear stratified ocean model of the equatorial undercurrent. Phil. Trans. Roy. Soc. London, *A298,* 603–635.

Mellor, G. L., C. R. Mechoso and E. Keto. 1982. A diagnostic calculation of the general circulation of the Atlantic Ocean. Deep-Sea Res., *29,* 1171–1192.

Mertz, G. and D. G. Wright. 1992. Interpretations of the JEBAR term. J. Phys. Oceanogr., *22,* 301–305.

Munk, W. H. 1950. On the wind-driven ocean circulation. J. Meteor., *7,* 79–93.

Niiler, P. P. and W. S. Richardson. 1973. Seasonal variability of the Florida Current. J. Mar. Res., *31,* 144–167.

Rhines, P. B. and W. R. Young. 1982. A theory of the wind-driven circulation I. Mid-ocean gyres. J. Mar. Res., *40* (Suppl.), 559–596.

Rooth, C., H. Stommel and G. Veronis. 1978. On motion in steady layered geostrophic models. J. Oceanogr. Soc. Japan, *34,* 265–267.

Salmon, R. 1986. A simplified linear ocean circulation theory. J. Mar. Res., *44,* 695–711.

—— 1992. A two-layer Gulf Stream over a continental slope. J. Mar. Res., *50,* 341–365.

—— 1994. Generalized two-layer models of ocean circulation. J. Mar. Res., *52,* 865–908.

Sarkisyan, A. S. 1969. Deficiencies of barotropic models of ocean circulation. Izv. Acad. Sci. USSR Atmos. Oceanic Phys. (English translation), *5,* 466–474.

—— 1977. The diagnostic calculations of a large-scale oceanic circulation, *in* The Sea, Vol. 6, E. D. Goldberg, I. N. McCave, J. J. O'Brien and J. H. Steele, eds., Wiley, New York, 1049 pp.

Sarkisyan, A. S. and V. F. Ivanov. 1971. Joint effect of baroclinicity and bottom relief as an important factor in the dynamics of sea currents. Izv. Acad. Sci. USSR Atmos. Oceanic Phys. (English translation), *7,* 173–188.

Schulman, E. E. and P. P. Niiler. 1970. Topographic effects on the wind-driven ocean circulation. Geophys. Fluid Dyn., *1,* 439–462.

Sekine, Y. and K. Kutsuwada. 1994. Seasonal variation in volume transport of the Kuroshio south of Japan. J. Phys. Oceanogr., *24,* 261–272.

Stommel, H. 1948. The westward intensification of wind-driven ocean currents. Trans. Am. Geophys. Union, *29,* 202–206.

Stommel, H., A. B. Arons and A. J. Faller. 1958. Some examples of stationary planetary flow patterns in bounded basins. Tellus, *10,* 179–187.

Veronis, G. 1973. Model of world ocean circulation: I. Wind-driven, two-layer. J. Mar. Res., *31,* 228–288.

—— 1981. Dynamics of large-scale ocean circulation, *in* Evolution of Physical Oceanography, B. A. Warren and C. Wunsch, eds., The MIT Press, Cambridge and London, 623 pp.

Welander, P. 1959. On the vertically integrated mass transport in the oceans, *in* The Atmosphere and the Sea in Motion, B. Bolin, ed., The Rockefeller Institute Press, New York, 509 pp.

—— 1966. A two-layer frictional model of wind-driven motion in a rectangular oceanic basin. Tellus, *18,* 54–62.

Yamagata T. and S. G. H. Philander. 1985. The role of damped equatorial waves in the oceanic response to winds. J. Oceanogr. Soc. Japan, *41,* 345–357.

Received: *14 April, 1995;* revised: *31 October, 1995.*